

GSVNET: GUIDED SPATIALLY-VARYING CONVOLUTION FOR FAST SEMANTIC SEGMENTATION ON VIDEO

Shih-Po Lee, Si-Cun Chen, Wen-Hsiao Peng

National Yang Ming Chiao Tung University, Taiwan
{splee, sicun.mapl.cs09, wpeng}@nycu.edu.tw

ABSTRACT

This paper addresses fast semantic segmentation on video. Video segmentation often calls for real-time, or even faster than real-time, processing. One common recipe for conserving computation arising from feature extraction is to propagate features of few selected keyframes. However, recent advances in fast image segmentation make these solutions less attractive. To leverage fast image segmentation for furthering video segmentation, we propose a simple yet efficient propagation framework. Specifically, we perform lightweight flow estimation in 1/8-downscaled image space for temporal warping in segmentation outpace space. Moreover, we introduce a guided spatially-varying convolution for fusing segmentations derived from the previous and current frames, to mitigate propagation error and enable lightweight feature extraction on non-keyframes. Experimental results on Cityscapes and CamVid show that our scheme achieves the state-of-the-art accuracy-throughput trade-off on video segmentation.

1. INTRODUCTION

Video semantic segmentation is a compute-intensive vision task. It aims at classifying pixels in video frames into semantic classes. This task often has real-time or even faster than real-time requirements in data-center applications, in order to process hours-long videos in a much shorter time. The ever increasing video resolution in both spatial and temporal dimensions makes real-time processing even more challenging.

A simple approach to video segmentation is to adopt image-based processing; that is, to process individual video frames independently using an off-the-shelf image segmentation network. This approach was once considered prohibitively expensive, given that most image segmentation networks, like DeepLabv3+ [1], usually optimized the feature extraction for segmentation accuracy rather than throughput.

To address the prolonged feature extraction, several fast video segmentation frameworks are proposed. One common recipe is to propagate features of few selected keyframes, in order to conserve computation for feature extraction on subsequent non-keyframes [2, 3]. This is motivated by the high correlation between consecutive video frames. Due to

the evolution of video content in the temporal dimension, some [4, 5] additionally introduce lightweight feature extraction, followed by fusion of spatio-temporal features [4, 5], for non-keyframes to cope with scene changes or dis-occlusion. Others propose adaptive keyframe selection [6, 5] or bi-directional feature propagation [7] for alleviating error propagation. Meanwhile, Xu *et al.* [6] perform adaptive inference for cropped regions with scene changes.

However, recent advances in fast image segmentation [8, 9, 10] make video-based solutions less attractive. For example, BiSeNet [8] and SwiftNet [9] can now process high-definition (2048×1024) videos at 40 to 60 frames per second on modern graphics processing units (GPU) while achieving reasonably good segmentation accuracy. A question that arises is whether video-based approaches can benefit from these advanced image segmentation networks. The answer relies crucially on how to address the following challenges. First, the increasing spatial resolution of videos may render optical flow estimation too expensive. Second, the excessive amount of channels in feature space may make the propagation of features time-consuming. Third, the feature extraction for non-keyframes has to be even more lightweight. Lastly, errors resulting from imperfect flow estimation and feature extraction may be propagated along the temporal dimension.

To tackle these issues, we propose a simple yet efficient propagation framework, termed GSVNet, for fast semantic segmentation on video. Our contributions include: (1) to conserve computation for temporal propagation, we perform lightweight flow estimation in 1/8-downscaled image space for warping in segmentation outpace space; and (2) to mitigate propagation error and enable lightweight feature extraction on non-keyframes, we introduce a guided spatially-varying convolution for fusing segmentations derived from the previous and current frames.

Experimental results on Cityscapes [11] show that when working with BiSeNet [8] and SwiftNet [9], our scheme can process up to 142 high-definition (2048×1024) video frames per second on GTX 1080Ti with 71.8% accuracy in terms of Mean Intersection over Union (mIoU). It achieves the state-of-the-art accuracy-throughput trade-off on video segmentation and can readily work with any off-the-shelf fast image segmentation network.

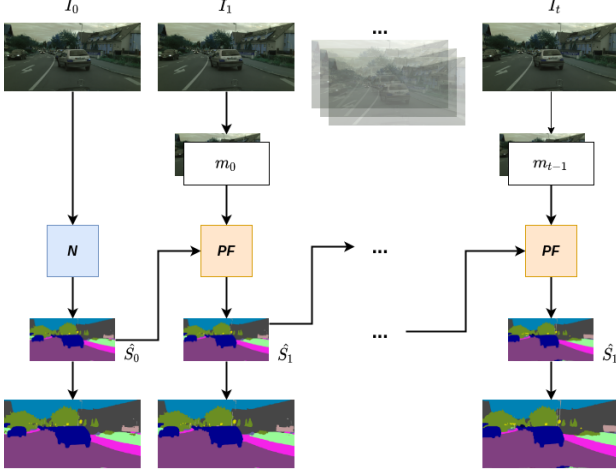


Fig. 1: Illustration of our proposed propagation framework, where m_i is the optical flow map, N denotes the image-based segmentation network and \mathcal{PF} indicates our propagation network.

2. RELATED WORK

Image Semantic Segmentation: Image semantic segmentation models [1, 12] have achieved great success in segmentation accuracy by incorporating sophisticated feature extractors and task decoders [1, 12]. To achieve better accuracy-throughput trade-offs, recent research [13, 8, 10] has been focused on making feature extractors lightweight and less sensitive to the adaptation of input resolution. To this end, Yu *et al.* [8] introduce a cost-effective feature extractor by including a spatial path for preserving spatial details and a context path for capturing contextual information in a wide receptive field. In another attempt, Orsic *et al.* [9] take the advantage of transfer learning by using pre-trained encoder on ImageNet and adopting a simple upsampling decoder with lateral connections.

Video Semantic Segmentation: Efficient video segmentation is another active research area. Unlike images, consecutive video frames usually have a high correlation or similarity. To conserve computation for feature extraction, several works leverage the temporal correlation between video frames to reuse features of selected keyframes on non-keyframes. Shelhamer *et al.* [2] employ features at different stages of the network from previous frames. For feature propagation, Zhu *et al.* [3] use optical flow estimated by a flow network, while Li *et al.* [5] adopt spatially variant convolution. [4, 5] additionally introduce lightweight feature extraction for non-keyframes together with spatio-temporal feature fusion, to reduce error propagation arising from scene changes or warping errors. However, the emergence of lightweight image segmentation calls for a careful rethink of these strategies. Specifically, the feature extraction on non-keyframes must be even more lightweight and the extracted features must be used to their fullest potential to mitigate error propagation.

3. METHOD

This work addresses the problem of efficient semantic segmentation on video. Given an input video consisting of a set $\{I_t\}_{t=0}^{N-1}$ of video frames, each being of dimension $3 \times H \times W$, our task is to predict for every video frame I_t its downsampled, semantic segmentation $\hat{S}_t \in \mathbb{R}^{C \times H/8 \times W/8}$ with C classes, aiming to strike a good balance between *accuracy* and *throughput*. Following common practice, the final segmentation is obtained by upsampling \hat{S}_t to the full resolution, where the segmentation accuracy is measured.

3.1. System Overview

Fig. 1 illustrates our proposed method for efficient semantic segmentation on video. The process begins by segmenting the first keyframe to obtain its semantic segmentation \hat{S}_0 with an image-based segmentation network N . Our propagation framework \mathcal{PF} then propagates temporally the segmentation \hat{S}_0 (respectively, \hat{S}_{t-1}) of the previous step to assist in predicting the segmentation \hat{S}_1 (respectively, \hat{S}_t) for the current non-keyframe I_1 (respectively, I_t). The process repeats until the next keyframe is reached.

3.2. Spatiotemporal Propagation Framework

Fig. 2 shows the pipeline of our segmentation propagation framework \mathcal{PF} . Starting with the downsampled segmentation $\hat{S}_{t-1} \in \mathbb{R}^{C \times H/8 \times W/8}$ for the previous frame I_{t-1} , we (1) perform temporal (backward) warping of \hat{S}_{t-1} based on the optical flow $m_t \in \mathbb{R}^{2 \times H/8 \times W/8}$ to arrive at an initial estimate $\hat{S}_t^- \in \mathbb{R}^{C \times H/8 \times W/8}$ of the downsampled segmentation for the current frame I_t . It is obvious that not every semantic prediction in \hat{S}_t^- is reliable. The errors can propagate along the temporal dimension through the warping process. Moreover, the optical flow m_t may be error-prone due to dis-occlusion or imperfect flow estimation. We thus (2) refine the warped segmentation \hat{S}_t^- by applying a *guided spatially-varying* convolution. This is achieved in three sequential steps. The first convolves the \hat{S}_t^- with several *ideal-delay* kernels $\theta_1, \theta_2, \dots, \theta_D$, yielding $\{f_{t,d}^s\}_{d=1}^D, f_{t,d}^s \in \mathbb{R}^{C \times H/8 \times W/8}$. The second arranges $\{f_{t,d}^s\}_{d=1}^D$ together with a crude estimate $f_t^i \in \mathbb{R}^{C \times H/8 \times W/8}$ of the current frame’s segmentation from a lightweight network into C chunks, each concatenating the channels of the same index from $\{f_{t,d}^s\}_{d=1}^D$ and f_t^i . The last applies a spatially-varying 1×1 convolution across the channels of each of these C chunks, with their results concatenated together to form our downsampled estimate $\hat{S}_t \in \mathbb{R}^{C \times H/8 \times W/8}$ of the current frame’s segmentation.

3.3. Temporal Segmentation Warping

This very first step performs temporal warping of \hat{S}_{t-1} to arrive at an initial estimate \hat{S}_t^- of the current frame’s segmentation. In symbols, we have

$$\hat{S}_t^-(c, x, y) = \hat{S}_{t-1}(c, x + m_t^{(x)}(x, y), y + m_t^{(y)}(x, y)), \forall c \in C \quad (1)$$

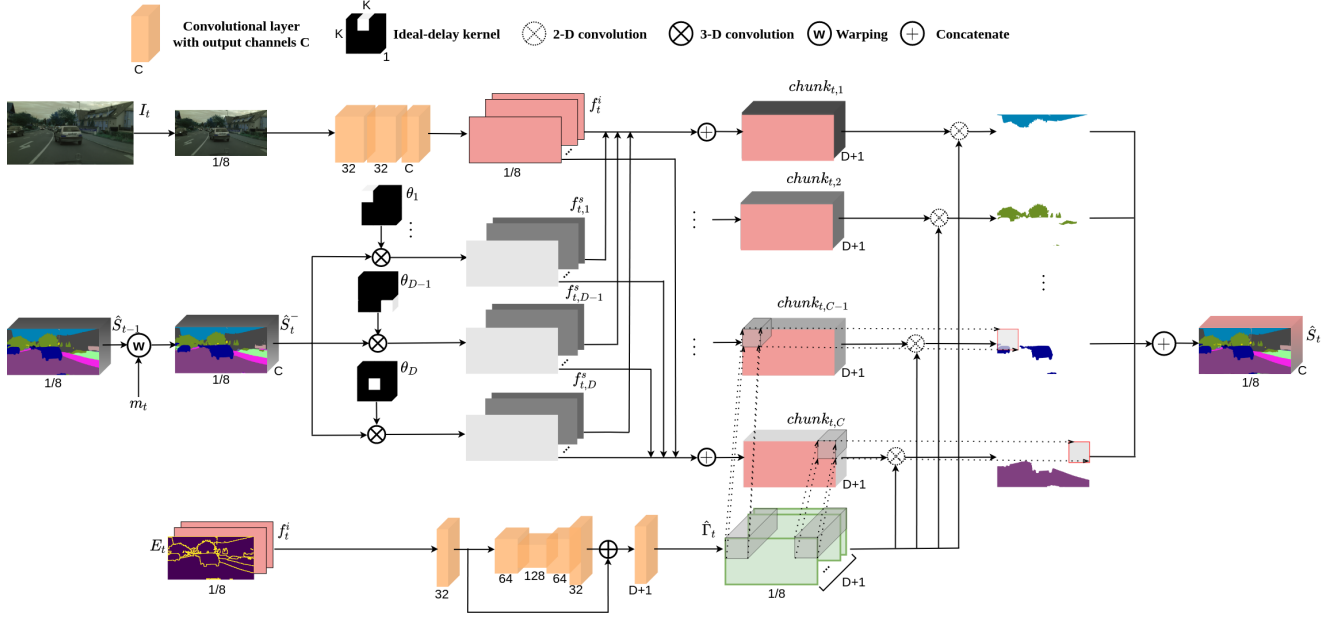


Fig. 2: Architecture diagram of the proposed propagation network $\mathcal{P}\mathcal{F}$.

where $(x, y), 1 \leq x \leq W/8, 1 \leq y \leq H/8$ denotes pixel locations in the downsampled segmentation and $m_t = (m_t^{(x)}, m_t^{(y)})$ is the optical flow describing the backward motion from I_t to I_{t-1} also in the downsampled domain, and is estimated by a lightweight optical flow network O based on the hierarchical feature fusion block. More details of this flow network can be found in the supplementary document. Performing temporal warping in the 1/8-downsampled domain is motivated by two observations. First, lowering the spatial resolution can significantly reduce the runtime costs of both optical flow estimation and temporal warping. Second, the 1/8 downscaling factor is chosen empirically to match common practice in most segmentation network design that the final high-resolution segmentation is usually recovered by interpolating the network output by a factor of 8.

3.4. Guided Spatially-Varying Convolution

To correct unreliable segmentation predictions in \hat{S}_t^- , we resort to a guided spatially-varying filtering. This operation serves as a means to propagate *spatially* within \hat{S}_t^- the segmentation predictions from reliable regions to unreliable ones. Apparently, in what direction the propagation should be performed to correct the erroneous prediction at a pixel depends on the error pattern in its local neighborhood. As such, our filtering kernel is designed to be both context- and pixel-adaptive.

3.4.1. Spatial Propagation with Ideal-delay Kernels

Such spatial propagation starts by convolving the temporally warped segmentation \hat{S}_t^- with several ideal-delay kernels $\theta_1, \theta_2, \dots, \theta_D$. As a result of the convolution, each of these

kernels shifts the \hat{S}_t^- channel-wise by one pixel or more in a certain direction. When viewed from each pixel's perspective, these shifting operations line up its surrounding semantic predictions as potential candidates for propagation. For implementation, we consider each ideal-delay kernel as a 3-D tensor of size $1 \times K \times K$, where K indicates the propagation range measured in the maximum horizontal or vertical displacement of the unit impulse from the origin. It is then convolved with \hat{S}_t^- , also regarded as a 3-D tensor, using 3-D convolution \otimes to get $f_{t,d}^s = \hat{S}_t^- \otimes \theta_d$, where $f_{t,d}^s \in \mathbb{R}^{C \times H/8 \times W/8}$, $d = 1, 2, \dots, D$.

3.4.2. Lightweight Intra-frame Segmentation

Recognizing that there may be areas in a video frame where new image contents emerge or our spatial propagation may not work well, we further develop a lightweight network φ for segmentation in these areas. The former is also known as the dis-occluded areas; the latter is because our spatial propagation is susceptible to the errors of the previous frame's segmentation and the optical flow estimation. The module is showed in the upper branch of Fig. 2. Since these areas normally represent only a small percentage of pixels in a video frame, we design φ for low complexity, with its prediction accuracy focused on those error-prone areas. Our current implementation comprises only 3 convolutional layers with kernel size 3×3 without resolution downscaling. As shown in Fig. 2, it takes as input the 1/8-downsampled current video frame and outputs the segmentation $f_t^i = \varphi(\hat{S}_t^-)$, $f_t^i \in \mathbb{R}^{C \times H/8 \times W/8}$.

3.4.3. Guided Dynamic Filtering

Given $\{f_{t,d}^s\}_{d=1}^D$ and f_t^i from the previous two steps, the guided dynamic filtering forms a semantic prediction of ev-

ery pixel by spatially-varying 1×1 filtering. To proceed, we first organize $\{f_{t,d}^s\}_{d=1}^D$ and f_t^i into C chunks. Each chunk concatenates the channels of the same semantic class from $\{f_{t,d}^s\}_{d=1}^D$ and f_t^i ; that is, the resulting channels of a chunk correspond to semantic predictions of the same class yet shifted spatially from \hat{S}_t^- in different directions. We then use a guiding network G to produce the 1×1 kernel for every pixel. In particular, this kernel varies from one pixel location to another, determining dynamically how the spatial propagation is conducted at every pixel location or whether the intra-frame segmentation should be weighted more heavily.

The process is illustrated in the lower and right parts of Fig. 2. For implementation, the guiding network $\Gamma_t = G(f_t^i, E_t)$ takes as inputs f_t^i and E_t , where $E_t = \sigma(\hat{S}_t^- \otimes M)$ is an edge map derived from convolving \hat{S}_t^- with a Laplacian kernel M . In particular, before the convolution, we take the argmax operation with respect to \hat{S}_t^- to keep only the structure information inherent in the segmentation map. The output of the convolution is further passed through a Sigmoid function σ to clip the edge response. This design is inspired by the observation that \hat{S}_t^- tends to be erroneous at the object boundaries and in regions where the structure contour of \hat{S}_t^- is inconsistent with that of f_t^i , which captures rough semantic predictions. Finally, the network output $\Gamma_t \in \mathbb{R}^{(D+1) \times H/8 \times W/8}$ is the 1×1 kernel for every pixel location (x, y) , $1 \leq x \leq W/8, 1 \leq y \leq H/8$. The filtering of every chunk then follows by evaluating

$$\hat{S}_{t,c}(x, y) = \hat{\Gamma}_t(x, y) \odot \text{chunk}_{t,c}(x, y), \forall c, x, y \quad (2)$$

where $\hat{\Gamma}_t(x, y)$ denotes the normalized kernel at (x, y) that has a unity gain across channels and \odot is the inner product. The filtered results, when pooled together, form the final segmentation output \hat{S}_t .

We train the propagation framework \mathcal{PF} end-to-end. The training objective involves an ordinary cross-entropy loss imposed on the final segmentation output.

4. EXPERIMENTS

4.1. Setup

Datasets: We validate our method on Cityscapes [11] and CamVid [14], the datasets for scene understanding. Cityscapes includes video snippets of urban scenes, of which 2975/500/1525 are for training/validation/test. Each snippet of resolution 2048×1024 is 30 frames long, with only the 20th frame annotated. CamVid has 4 video sequences. In each video, only one frame in every 30 frames is annotated, leading to a total of 701 labeled video frames of size 960×720 . Among these video frames, 367/101/233 are for training/validation/test.

Accuracy Metrics: For evaluating the segmentation accuracy, we follow the protocol in [3, 4] to measure the Mean Intersection over Union (mIoU) over l image pairs $(20-i, 20)$

in every snippet with $i = 0, 1, \dots, l-1$. For each image pair (a, b) , we propagate the segmentation for frame a (keyframe) recursively to frame b (non-keyframe). The mIoU measured this way is known as the *average* mIoU. We also report the *minimum* mIoU measured with respect to the non-keyframe farthest away from the keyframe in every snippet, i.e. the non-keyframe that is expected to be impacted the most by error propagation in the temporal dimension. Unless otherwise stated, the keyframe interval l is defaulted to 5. Note that all the mIoU numbers reported are measured at full resolution.

Complexity Metrics: For complexity assessment, we report the throughput in *frames per second* (FPS) on GTX 1080Ti, the number of network parameters in bytes, and the average number of *floating-point operations per second* (FLOPS) over a keyframe interval.

Implementation Details: We implement our network on PyTorch, and use pre-trained SwiftNet-R18 [9], termed SN-R18 or BiSeNet-R18, termed BN-R18, as the segmentation model for keyframes. Both SN-R18 and BN-R18 adopt the ResNet-18 backbone. At inference time, the size of the keyframe is downscaled for the best accuracy-throughput trade-off. By the same token, our propagation module operates at one-eighth the resolution of the input video frame, followed by an interpolation of the segmentation output to the full resolution for mIoU measurement. Similar to [3, 4], we train our network for keyframe intervals ranging from 1 to 5. We use stochastic gradient descent (SGD) with momentum 0.9 and a learning rate of 0.002, which is decreased by a factor of 0.992 every 100 iterations. We set the batch size to 8 and the weight decay to 0.0005. Our model, exclusive of the pre-trained SwiftNet-R18 or BiSeNet-R18 for keyframe segmentation, is then trained end-to-end over image patches cropped from the input image. Each patch is three quarters of the input size.

4.2. Results

Accuracy-throughput Trade-off: Table 1 compares the accuracy-throughput trade-offs of the competing methods. As shown, at FPS around 130, Ours-BN-R18 ($l = 4$) outperforms BiSeNet-R18 with input size 0.5 by 2.3% mIoU. Likewise, Ours-SN-R18 ($l = 4$) surpasses SwiftNet-R18 with input size 0.5 by 3.1% mIoU. Comparing with the video-based methods like [2, 4, 6], our scheme achieves much higher FPS and mIoU. In particular, Ours-SN-R18 ($l = 2$) outpaces considerably [5, 15], which target also high throughput, in FPS at the cost of a modest drop in mIoU. Results on Camvid [14] (Table 3) show that our method runs faster than the image-based schemes [8] while achieving higher or comparable mIoU. It is to be noted that the other video-based schemes can hardly compete with ours in FPS, although [15] has higher mIoU due to the use of better backbones.

Network Parameters and FLOPS: Table 2 compares the number of network parameters and FLOPS. As can be seen, our scheme introduces 1.6M additional network parame-

Table 1: Accuracy and throughput comparison on Cityscapes dataset. The l specifies the keyframe interval. The input size indicates the downscaling factor for keyframes in the video-based schemes or for input images in the image-based schemes.

Method	Input size	Avg. mIoU	FPS
CLK [2]	1.0	64.4	6.3
LVS-LLS [5]	1.0	75.9	8.4
Accel-R18 [4]	1.0	72.1	2.2
DVSNet [6]	1.0	63.2	30.3
TD-BN-R18 [15]	1.0	75.0	47
Fast-SCNN [10]	0.5	68.6	123.5
BiSeNet-R18 [8]	0.75	73.7	62
BiSeNet-R18 [8]	0.5	68.9	131
SwiftNet-R18 [9]	0.75	74.4	63.2
SwiftNet-R18 [9]	0.5	68.7	134
Ours-BN-R18 ($l=2$)	0.75	72.9	98.5
Ours-BN-R18 ($l=3$)	0.75	72.0	123.4
Ours-BN-R18 ($l=4$)	0.75	71.2	140
Ours-SN-R18 ($l=2$)	0.75	73.6	100
Ours-SN-R18 ($l=3$)	0.75	72.6	125
Ours-SN-R18 ($l=4$)	0.75	71.8	142

Table 2: Complexity comparison in terms of network parameters, FLOPS and FPS.

Method	Input size	FPS	Key params	Non-key params	FLOPS
BiSeNet-R18	0.75	62.0	49.0M	-	58.0G
SwiftNet-R18	0.75	63.2	47.2M	-	58.5G
SwiftNet-R18	0.5	134	47.2M	-	26.0G
Ours-SN-R18 ($l=4$)	0.75	142	47.2M	1.6M	16.7G

ters for segmenting non-keyframes, representing less than 3.3% additional overhead relative to image-based segmentation with SwiftNet-R18 or BiSeNet-R18. It achieves the least number of FLOPS, with a FPS of 142 and 71.8% average mIoU. In particular, the FLOPS of our scheme is variable depending on the keyframe interval. On average, a non-keyframe requires 2.8G FLOPS, as compared to 58.5G FLOPS for processing a keyframe with SwiftNet-R18 (0.75). As such, the higher the keyframe interval, the lower the FLOPS.

4.3. Ablation Experiments

This section aims at dissecting our design to understand better the contributions of each component.

Using Lightweight Flow Estimation and Feature Extraction in A-R18: Fig. 3 shows that Accel-R18, when trained end-to-end with our lightweight flow estimation network and feature extractor (a scheme termed A-Lite), suffers from a significant mIoU drop, although its throughput is much improved (red vs. cyan curves). This stresses the novelty of our

Table 3: Accuracy and FPS comparison on CamVid test set.

Method	Input size	Avg. mIoU	FPS
Accel [4]	1.0	66.7	7.58
TD-PSP18 [15]	1.0	71.0	25
TD-PSP50 [15]	1.0	74.7	10
BiSeNet-R18 [8]	0.75	66.6	142
BiSeNet-R18 [8]	0.5	60.7	232
Ours-BN-R18 ($l=2$)	0.75	65.9	210
Ours-BN-R18 ($l=3$)	0.75	64.8	250

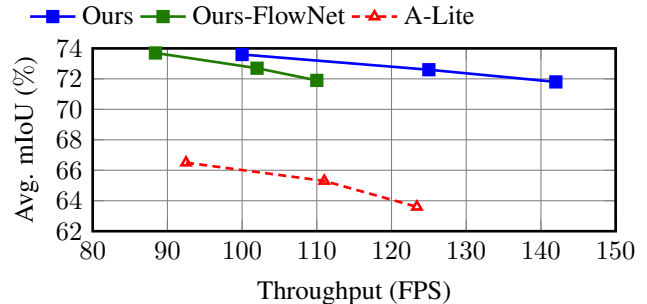


Fig. 3: Comparison of accuracy-throughput curves. A-Lite adopts the same flow network and feature extractor as ours. Ours-FlowNet uses FlowNet2s for flow estimation.

guided dynamic filtering. Also shown in Fig. 3 is that using FlowNet2s [16] in our framework has little impact on mIoU (blue vs. green curves). This however causes the throughput to reduce considerably, due to the prolonged runtime for flow estimation.

Discarding Intra Features: Intra features refer to the features extracted from the current frame. They serve the purposes of guiding the 1×1 dynamic filtering and refining the semantic predictions propagated from the previous frame. Table 4 shows that discarding these intra features causes the *minimum* mIoU to drop much faster along with the increasing keyframe interval, highlighting their necessity for mitigating error propagation.

4.4. Qualitative Evaluation

Fig. 4 presents qualitative evaluation. For a fair comparison, all the competing models are configured to have a similar throughput (120 to 140 FPS). Because of lightweight temporal propagation, video-based methods can afford higher-accuracy keyframe segmentation, e.g. SwiftNet-R18 (0.75) in our method and BiSeNet-R18 (0.75) in A-Lite. We adopt A-Lite instead of A-X39 for comparison as it is the only version of Accel that achieves a similar throughput to the others. It is seen that our method produces consistently better segmentations across video frames (see the poles especially in the top-left area) than SwiftNet-R18 (0.5). In addition, A-Lite suffers from seriously distorted object boundaries. More qualitative results can be found in our supplementary document.

Table 4: Accuracy comparison between models with and without the use of the current frame’s features (intra features). The accuracy is measured in minimum mIoU over a keyframe interval to emphasize the worst case.

Metric	Intra Feature	Keyframe interval				
		1	2	3	4	5
Min.	with	74.4	72.9	70.7	69.6	67.7
mIoU	without	74.4	72.1	69.1	67.4	65.1

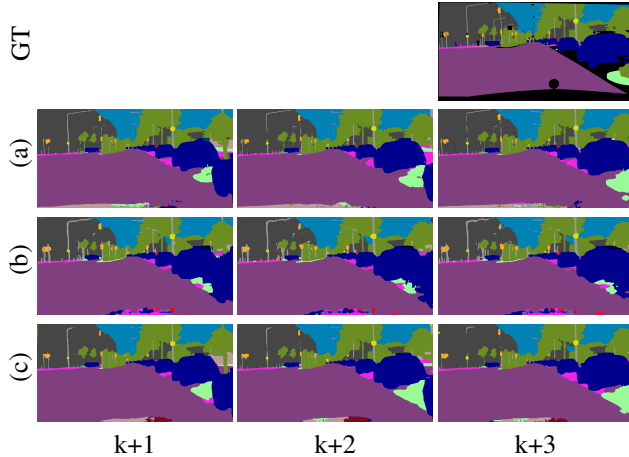


Fig. 4: Qualitative evaluation: (a) Ours-SN-R18 (0.75), (b) A-Lite, and (c) SwiftNet-R18 (0.5). From left to right, each column with index $k + n$ shows the segmentation results for a video frame that is n steps after the keyframe k . Note that only the last frame ($k+3$) has the ground-truth segmentation.

5. CONCLUSION

This paper presents a simple propagation framework for efficient video segmentation. We show that it is more cost-effective to perform warping in segmentation output space than in feature space. This also allows the propagation error to be minimized at each time step by our guided spatially-varying convolution. Our scheme has the striking feature of being able to work with any off-the-shelf fast image segmentation network to further video segmentation.

6. ACKNOWLEDGEMENT

We are grateful to the National Center for High performance Computing for GPU resources. This project is supported by MOST 108-2634-F-009-007 through Pervasive AL Research (PAIR) Labs, National Chiao Tung University, Taiwan.

7. REFERENCES

[1] Liang-Chieh Chen, Yukun Zhu, George Papandreou, Florian Schroff, and Hartwig Adam, “Encoder-decoder with atrous separable convolution for semantic image segmentation,” in *ECCV*, 2018.

[2] Evan Shelhamer, Kate Rakelly, Judy Hoffman, and Trevor Darrell, “Clockwork convnets for video semantic segmentation,” in *ECCV*, 2016.

[3] Xizhou Zhu, Yuwen Xiong, Jifeng Dai, Lu Yuan, and Yichen Wei, “Deep feature flow for video recognition,” in *CVPR*, 2017.

[4] Samvit Jain, Xin Wang, and Joseph E. Gonzalez, “Accel: A corrective fusion network for efficient semantic segmentation on video,” in *CVPR*, 2019.

[5] Yule Li, Jianping Shi, and Dahua Lin, “Low-latency video semantic segmentation,” in *CVPR*, 2018.

[6] Yu-Syuan Xu, Tsu-Jui Fu, Hsuan-Kung Yang, and Chun-Yi Lee, “Dynamic video segmentation network,” in *CVPR*, 2018.

[7] Samvit Jain and Joseph E Gonzalez, “Fast semantic segmentation on video using block motion-based feature interpolation,” in *ECCV Workshops*, 2018.

[8] Changqian Yu, Jingbo Wang, Chao Peng, Changxin Gao, Gang Yu, and Nong Sang, “Bisenet: Bilateral segmentation network for real-time semantic segmentation,” in *ECCV*, 2018.

[9] Marin Orsic, Ivan Kreso, Petra Bevandic, and Sinisa Segvic, “In defense of pre-trained imagenet architectures for real-time semantic segmentation of road-driving images,” in *CVPR*, 2019.

[10] Rudra P K Poudel, Stephan Liwicki, and Roberto Cipolla, “Fast-scnn: Fast semantic segmentation network,” in *BMVC*, 2019.

[11] Marius Cordts, Mohamed Omran, Sebastian Ramos, Timo Rehfeld, Markus Enzweiler, Rodrigo Benenson, Uwe Franke, Stefan Roth, and Bernt Schiele, “The cityscapes dataset for semantic urban scene understanding,” in *CVPR*, 2016.

[12] Hengshuang Zhao, Jianping Shi, Xiaojuan Qi, Xiaogang Wang, and Jiaya Jia, “Pyramid scene parsing network,” in *CVPR*, 2017.

[13] Sachin Mehta, Mohammad Rastegari, Anat Caspi, Linda Shapiro, and Hannaneh Hajishirzi, “Espnet: Efficient spatial pyramid of dilated convolutions for semantic segmentation,” in *ECCV*, 2018.

[14] Gabriel J. Brostow, Jamie Shotton, Julien Fauqueur, and Roberto Cipolla, “Segmentation and recognition using structure from motion point clouds,” in *ECCV*, 2008.

[15] Ping Hu, Fabian Caba, Oliver Wang, Zhe Lin, Stan Sclaroff, and Federico Perazzi, “Temporally distributed networks for fast video semantic segmentation,” in *CVPR*, 2020.

[16] Eddy Ilg, Nikolaus Mayer, Tonmoy Saikia, Margret Keuper, Alexey Dosovitskiy, and Thomas Brox, “FlowNet 2.0: Evolution of optical flow estimation with deep networks,” in *CVPR*, 2017.

Appendices

A. ACCURACY-THROUGHPUT TRADE-OFF

Fig. A5 compares the accuracy-throughput curves of the competing methods. To trade lower accuracy for higher throughput, the keyframe interval is altered from 1 to 5 for A-X39 and the two variants of our scheme¹, while for the image-based methods, the input image is downscaled by a factor of 1, 0.75, 0.6, and 0.5, followed by an interpolation of the segmentation output to the full resolution.

Fig. A6 presents more accuracy-throughput curves by choosing BiSeNet (1.0) and SwiftNet (1.0) for keyframe segmentation. This shows that our scheme can work with these image segmentation networks under different settings to offer a wide variety of accuracy-throughput trade-offs. As mentioned in the main paper, it can readily work with any off-the-shelf image segmentation network.

B. MORE ABLATION EXPERIMENTS

B.1. Replacing Ideal-delay Kernels with Learned Kernels.

Table A5 indicates that little gain can be achieved by replacing the 3×3 ideal-delay kernels with learned kernels. Our reasoning is that the same net effect may be obtained by adapting the following 1×1 dynamic convolution kernels.

B.2. Enlarging Ideal-delay Kernels.

Table A6 further shows that enlarging the size of the ideal-delay kernels, equivalently allowing longer-distance spatial propagation, brings modest mIoU gain at the cost of lower throughput. For this experiment, we learn the kernels end-to-end since for the 5×5 case, only 17 out of 25 possible ideal-delay patterns are used for initialization and for maintaining high FPS. We attribute the result to the fact that our flow propagation network operates in the 1/8-downscaled domain (cp. Fig. 6 in the main paper). The 3×3 kernel size covers already a large enough receptive field in the full-resolution image space.

B.3. Edge Map Analysis

In the main paper (Section 3.4.3 Guided Dynamic Filtering), we conjecture that the warped segmentation \hat{S}_t^- tends to be erroneous at the object boundaries and propose to provide the edge map E_t derived from \hat{S}_t^- as the guiding signal for dynamic filtering. Fig. A7 validates our conjecture by showing the high correlation between the edge map and the error map (indicating the segmentation errors on \hat{S}_t^-).

¹The keyframe interval 1 corresponds to image-based segmentation.

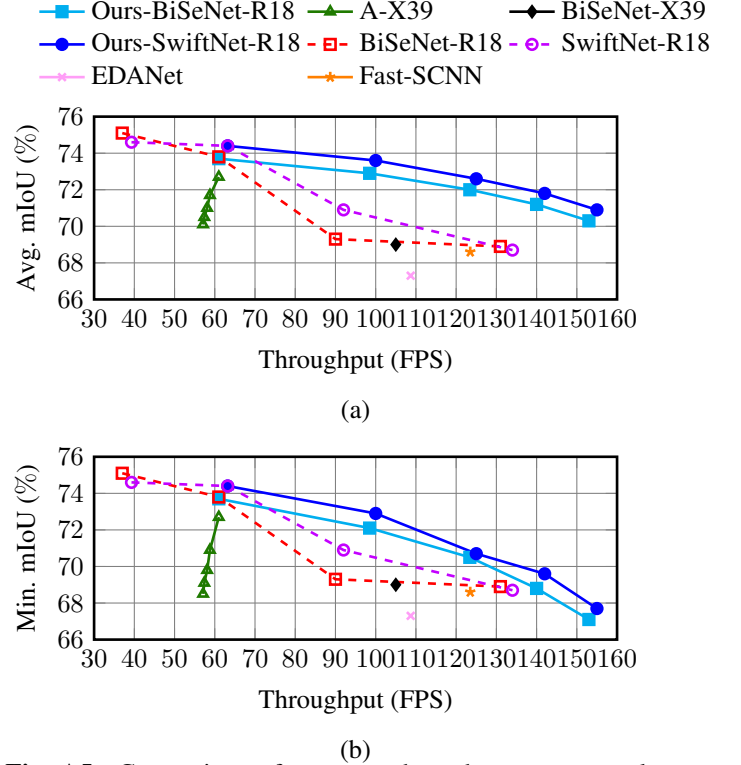


Fig. A5: Comparison of accuracy-throughput curves evaluated on Cityscapes validation set. The dashed lines correspond to image-based methods, where different accuracy-throughput trade-offs are achieved by adapting the input resolution with factors $\{1, 0.75, 0.6, 0.5\}$. EDANet, Fast-SCNN, and BiSeNet-X39 have an input scaling factor of 0.5, 1, and 0.75, respectively. The solid lines are video-based methods with a variable keyframe interval ranging from 1 to 5. For keyframe segmentation, ours-BiSeNet-R18 and ours-SwiftNet-R19 adopt BiSeNet-R18 (0.75) and SwiftNet-R18 (0.75), respectively. Likewise, A-X39 uses BiSeNet-R18 (0.75). The mIoU is evaluated at full resolution without regard to the input scaling factor.

C. LIGHTWEIGHT OPTICAL FLOW NETWORK

Fig. A8 details the architecture of our lightweight optical flow network O . It is built based on the hierarchical feature fusion block (HFFB), initially proposed for image super resolution. It first concatenates two input frames, I_{t-1} and I_t , followed by passing them through two 3×3 convolutional layers with stride 2. The resulting feature maps are then input to HFFB, which consists of 4 convolutional layers with dilation 1, 2, 4, and 8. The outputs of these convolutional layers are added and pooled hierarchically as illustrated in the figure. Finally, a 3×3 convolution is applied to get a downscaled flow map m_t , which is interpolated bilinearly to the resolution of one-eighth of the resolution of input image.

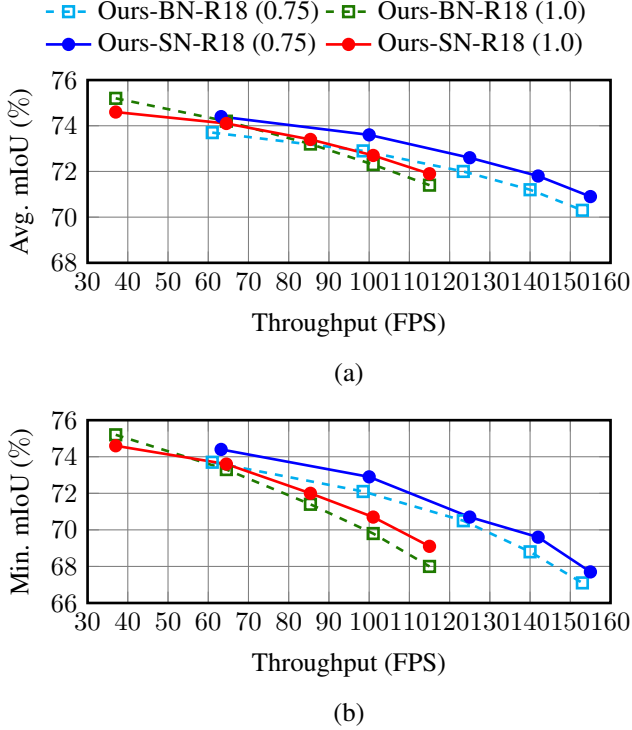


Fig. A6: Comparison of accuracy-throughput curves.

Table A5: Accuracy comparison between models with ideal-delay kernels and fine-tuned kernels for various keyframe intervals. **IDK:** Ideal-delay Kernel.

Metric	Scheme	Keyframe interval				
		1	2	3	4	5
Avg.	IDK	74.4	73.7	72.6	71.8	70.9
mIoU (%)	IDK+Finetune	74.4	73.6	72.6	71.8	70.9

D. INFERENCE RUNTIME

We apply a breakdown analysis of inference runtime on non-keyframe segmentation for A-X39 and our scheme in Fig. A9. The operation of non-keyframe segmentation is divided into four major parts: (1) optical flow estimation, (2) temporal warping in the feature or segmentation output space, (3) feature extraction from the current video frame, and (4) fusion of features or segmentation predictions. The runtimes of the three image-based methods (i.e. BiSeNet-X39, BiSeNet-R18, and SwiftNet-R18), which turn non-keyframes into keyframes for processing, are provided as monolithic quantities for comparison.

Several observations can be made from Fig. A9. First, A-X39 runs slower than all the image-based schemes, including BiSeNet-R18, i.e. the network used for keyframe segmentation in A-X39. Careful examination of A-X39 suggests that the additional operations needed for flow estimation and tem-

Table A6: Impact of the size of the ideal-delay kernels on accuracy and throughput. The mIoU is measured at the keyframe interval of 5.

Kernel size	# of filters	Avg. mIoU (%)	Min. mIoU (%)	FPS
3×3	9	70.9	67.7	155
5×5	17	71.1	67.9	144

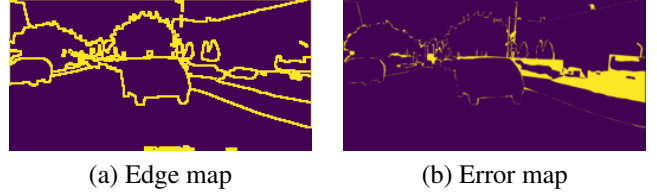


Fig. A7: Comparison between the edge map E_t and the error map, which indicates the errors on the temporally warped segmentation \hat{S}_t^- .

poral warping outweigh its runtime reduction from the use of the lightweight feature extractor in BiSeNet-X39. This explains our earlier finding that increasing non-keyframes in A-X39 leads to a slight decrease in throughput. Second, the runtime of A-X39 is still dominated by the feature extraction from the current frame. In contrast, our lightweight flow estimation network consumes only about one-third of the runtime of FlowNet2s [16] in A-X39. Moreover, performing temporal warping in the segmentation output space (ours) consumes much less time than in the feature space (A-X39). This is because temporal warping is a memory-intensive operation. Although the feature space in the present case has a spatial resolution (of 64×128) that is 4 times smaller than the segmentation output space (of size 128×256), it has $256/19=13.4$ times more channels, thereby leading to a 3.3 times increase in data to be moved around. Third, our feature extraction from the current frame represents only a small portion of the entire inference runtime, and is much simpler than that of A-X39. The improvement comes from downscaling the input image by a factor of 1/8 and using only 3 convolutional layers for feature extraction (cp. Fig. 2 in the main paper). Our ablation study, however, shows that without the guided dynamic filtering (Section 3.4 in the main paper), A-X39 cannot benefit from such a lightweight feature extractor. This also explains why the fusion of segmentation predictions through guided dynamic filtering constitutes a major source of complexity in our scheme.

Last but not least, the runtime distribution of our propagation framework justifies the aim of conserving computation for feature extraction from the current frame through exploiting temporal correlation between video frames.



Fig. A8: The architecture of our lightweight optical flow network. The red, blue, and green blocks each output 64, 32, and 2 channels, respectively. Except for the gray and green blocks, the other blocks all include 3×3 convolutional layers followed by batch normalization and LeakyReLU with a slope factor of 0.1.

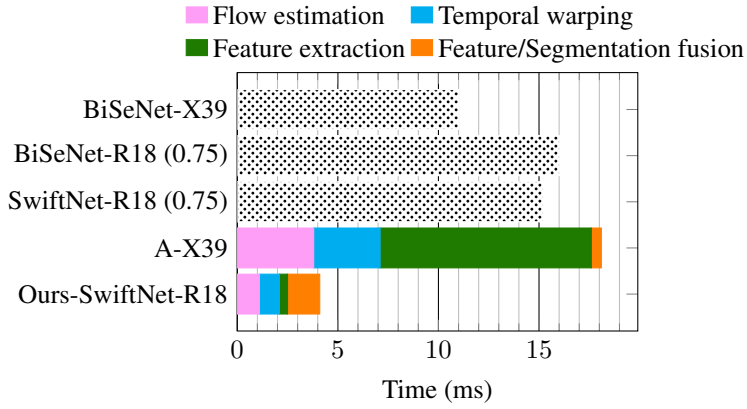


Fig. A9: A breakdown analysis of inference runtime.



(a)



(b)

Fig. A10: Qualitative evaluation on Cityscapes demo video ($k = 77$) for keyframe interval 4. (a) and (b) correspond to index k and $k + 1$ respectively, where $k + n$ denotes the n th non-keyframe following keyframe k



(a)



(b)

Fig. A11: Qualitative evaluation on Cityscapes demo video ($k = 77$) for keyframe interval 4. (a) and (b) correspond to index $k + 2$ and $k + 3$ respectively, where $k + n$ denotes the n th non-keyframe following keyframe k



(a)



(b)

Fig. A12: Qualitative evaluation on Cityscapes demo video ($k = 121$) for keyframe interval 4. (a) and (b) correspond to index k and $k + 1$ respectively, where $k + n$ denotes the n th non-keyframe following keyframe k

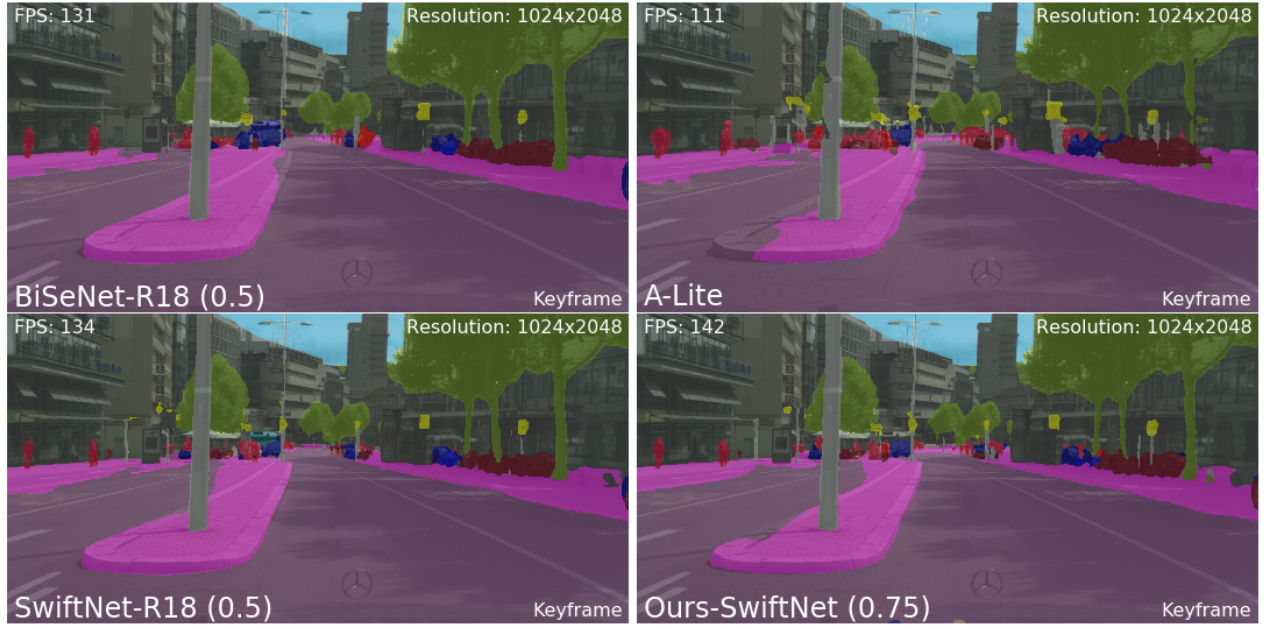


(a)

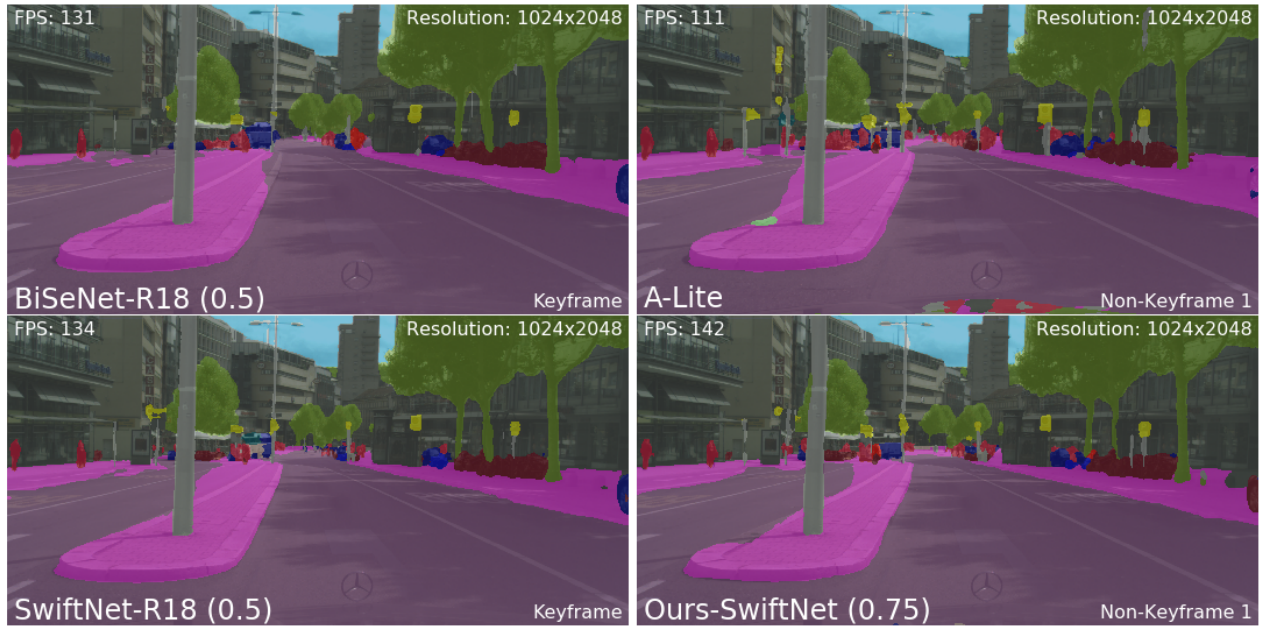


(b)

Fig. A13: Qualitative evaluation on Cityscapes demo video ($k = 121$) for keyframe interval 4. (a) and (b) correspond to index $k + 2$ and $k + 3$ respectively, where $k + n$ denotes the n th non-keyframe following keyframe k

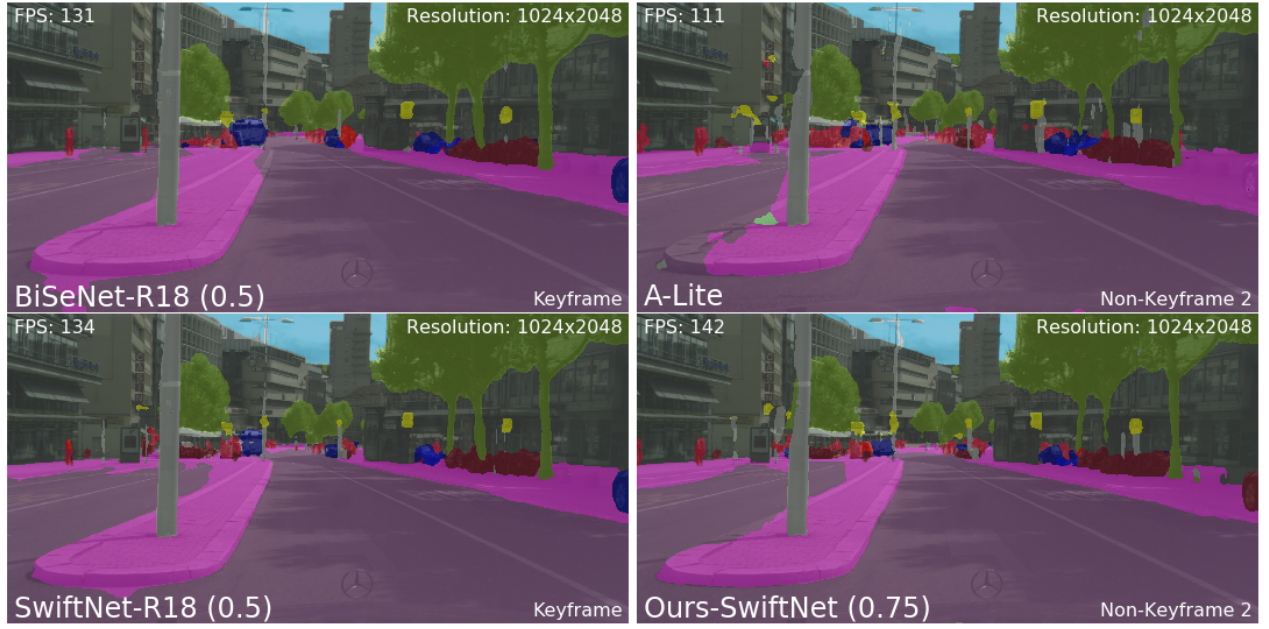


(a)

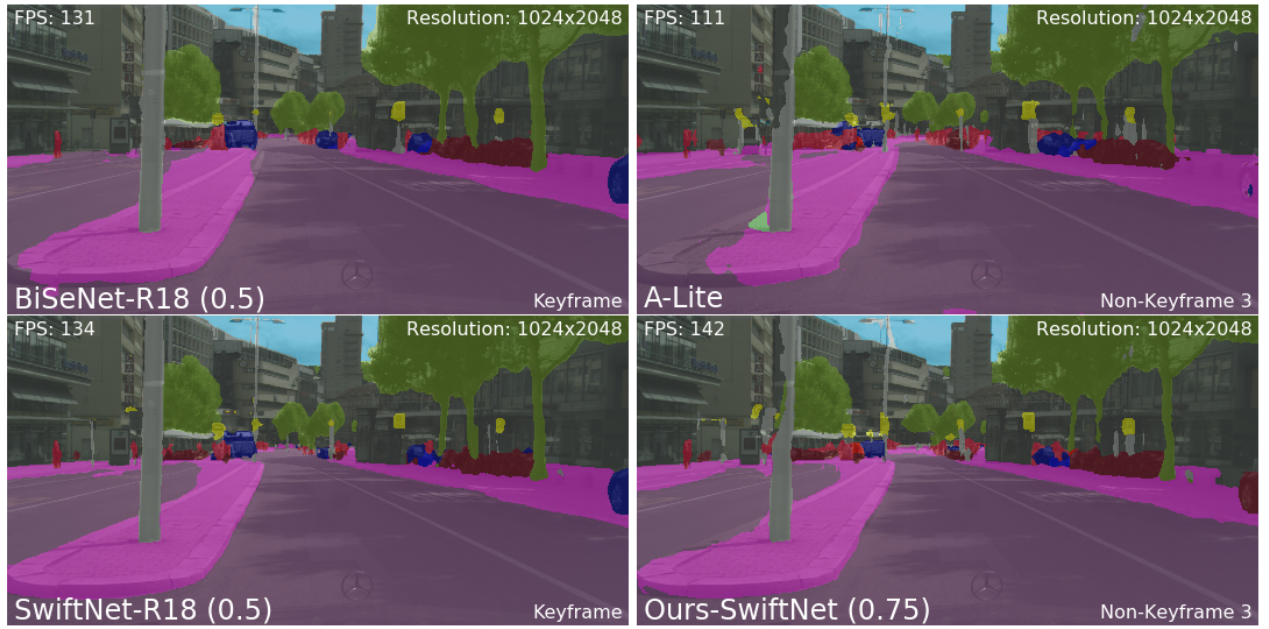


(b)

Fig. A14: Qualitative evaluation on Cityscapes demo video ($k = 261$) for keyframe interval 4. (a) and (b) correspond to index k and $k + 1$ respectively, where $k + n$ denotes the n th non-keyframe following keyframe k

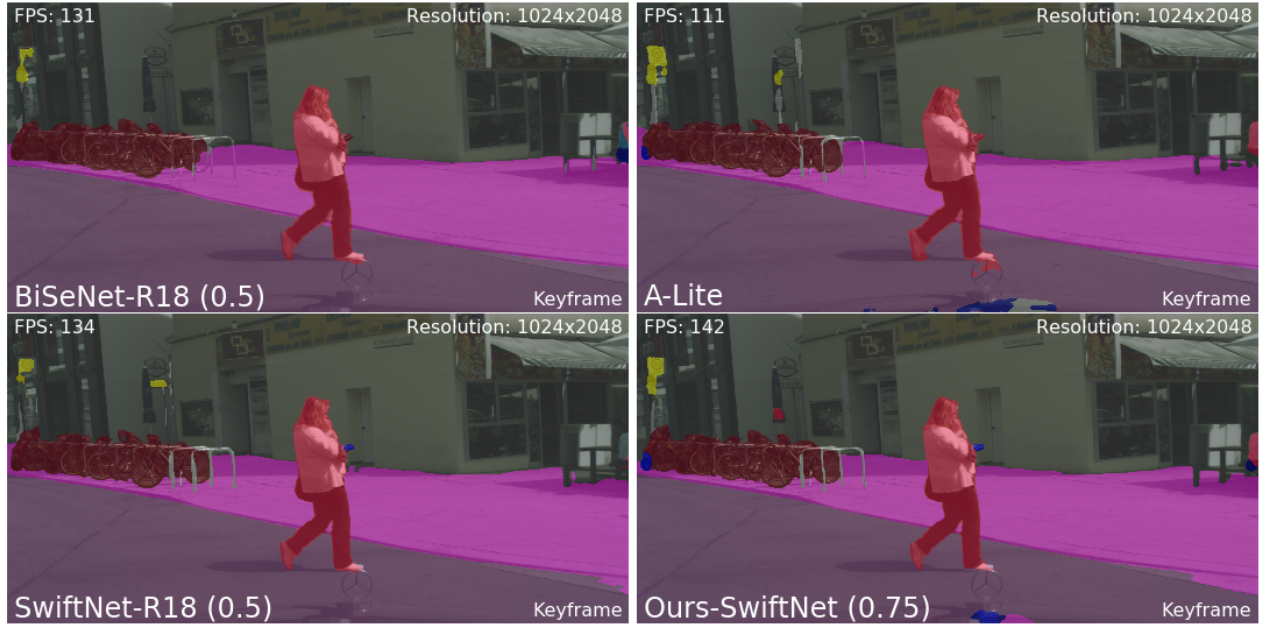


(a)

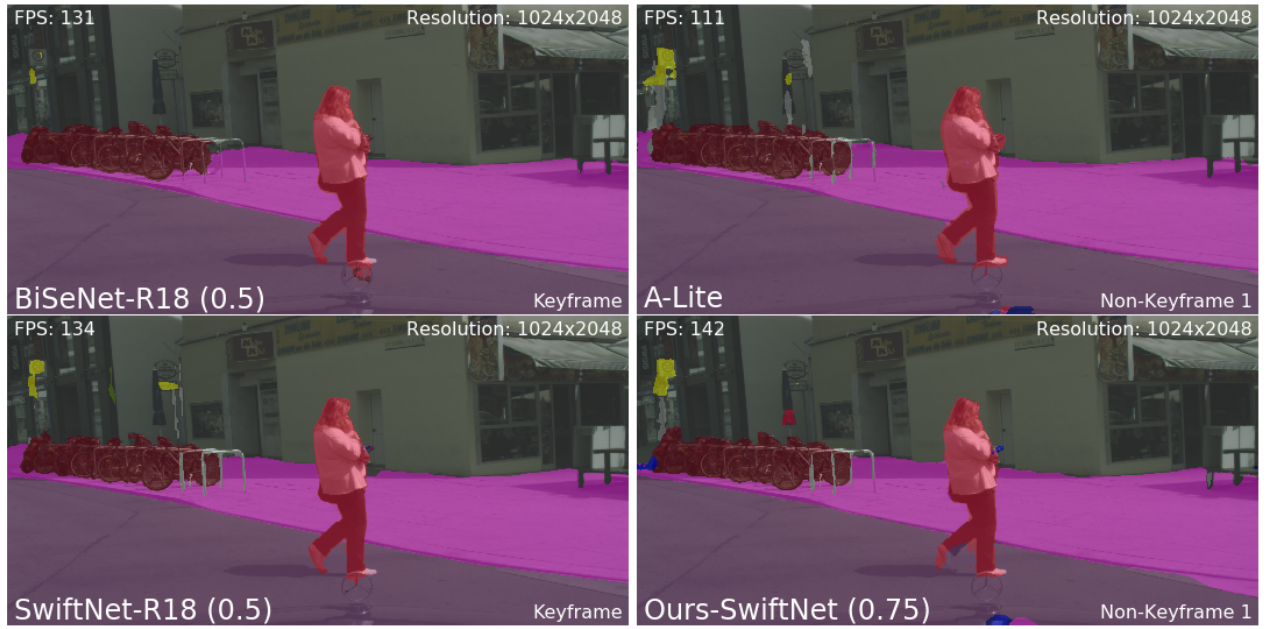


(b)

Fig. A15: Qualitative evaluation on Cityscapes demo video ($k = 261$) for keyframe interval 4. (a) and (b) correspond to index $k + 2$ and $k + 3$ respectively, where $k + n$ denotes the n th non-keyframe following keyframe k

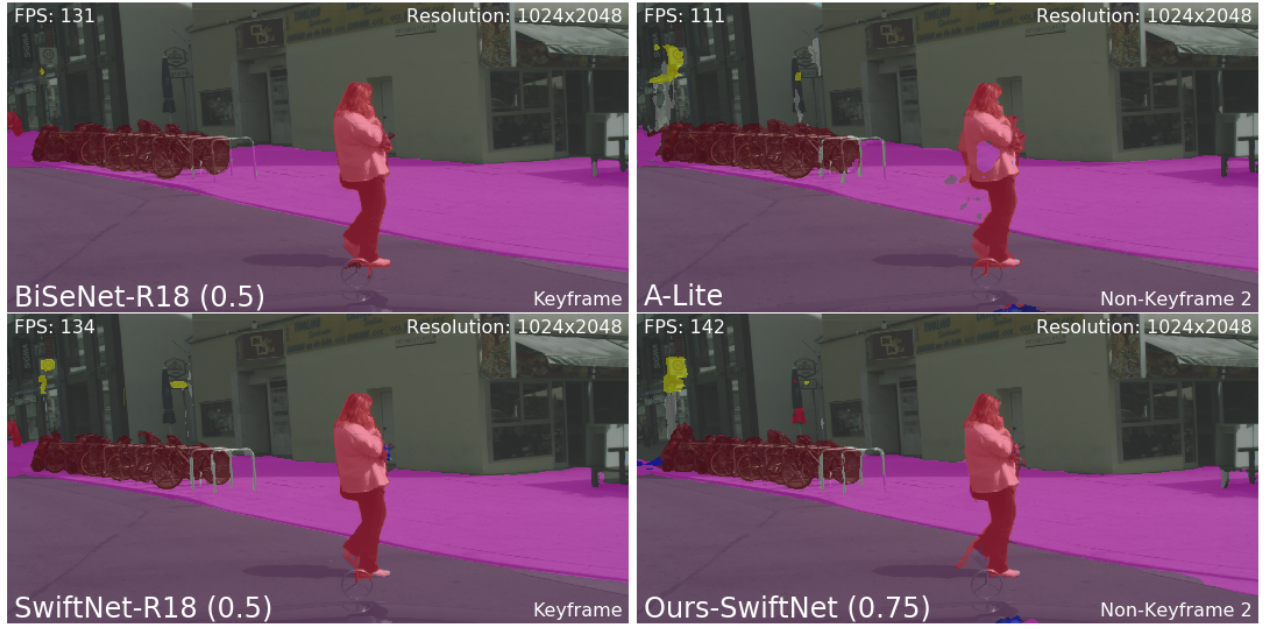


(a)

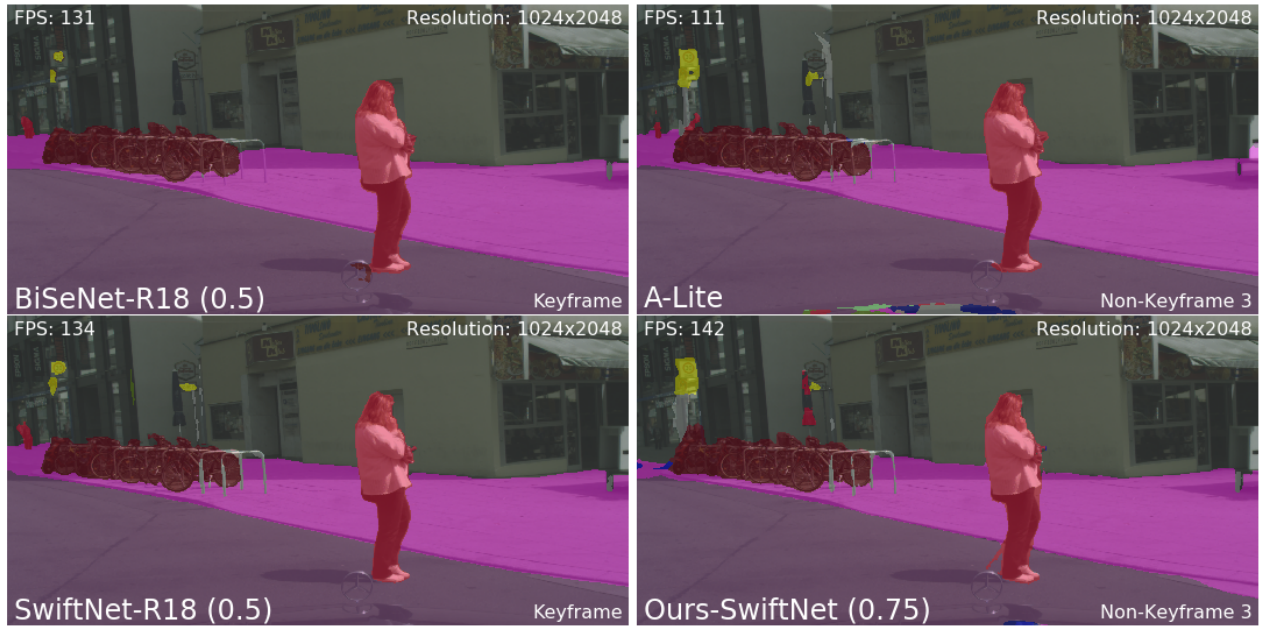


(b)

Fig. A16: Qualitative evaluation on Cityscapes demo video ($k = 481$) for keyframe interval 4. (a) and (b) correspond to index k and $k + 1$ respectively, where $k + n$ denotes the n th non-keyframe following keyframe k



(a)



(b)

Fig. A17: Qualitative evaluation on Cityscapes demo video ($k = 481$) for keyframe interval 4. (a) and (b) correspond to index $k + 2$ and $k + 3$ respectively, where $k + n$ denotes the n th non-keyframe following keyframe k